Ca^{2+}-activated Cl^- currents in the murine vomeronasal organ enhance neuronal spiking but are dispensable for male–male aggression

Received for publication, March 27, 2018, and in revised form, May 6, 2018 Published, Papers in Press, May 16, 2018, DOI 10.1074/jbc.RA118.003153

Jonas Münch[‡§¶], Gwendolyn Billig[‡§], Christian A. Hübner[‖], Trese Leinders-Zufall[1], Frank Zufall[**], and Thomas J. Jentsch[‡§‡‡2]**

*From the [‡]Leibniz-Forschungsinstitut für Molekulare Pharmakologie, D-13125 Berlin, Germany, the [§]Max-Delbrück-Centrum für Molekulare Medizin, D-13125 Berlin, Germany , the [¶]Graduate Program, Freie Universität Berlin, D-14195 Berlin, Germany , [‖]Institut für Humangenetik, Universitätsklinikum Jena, D-07747 Jena, Germany, the **Center for Integrative Physiology and Molecular Medicine, Saarland University, D-66421 Homburg, Germany, and the [‡‡]NeuroCure Cluster of Excellence, Charité Universitätsmedizin Berlin, D-10117 Berlin, Germany*

Edited by Roger J. Colbran

Ca^{2+}-activated Cl^- currents have been observed in many physiological processes, including sensory transduction in mammalian olfaction. The olfactory vomeronasal (or Jacobson's) organ (VNO) detects molecular cues originating from animals of the same species or from predators. It then triggers innate behaviors such as aggression, mating, or flight. In the VNO, Ca^{2+}-activated Cl^- channels (CaCCs) are thought to amplify the initial pheromone-evoked receptor potential by mediating a depolarizing Cl^- efflux. Here, we confirmed the co-localization of the Ca^{2+}-activated Cl^- channels anoctamin 1 (Ano1, also called TMEM16A) and Ano2 (TMEM16B) in microvilli of apically and basally located vomeronasal sensory neurons (VSNs) and their absence in supporting cells of the VNO. Both channels were expressed as functional isoforms capable of giving rise to Ca^{2+}-activated Cl^- currents. Although these currents persisted in the VNOs of mice lacking *Ano2*, they were undetectable in olfactory neuron-specific *Ano1* knockout mice irrespective of the presence of *Ano2*. The loss of Ca^{2+}-activated Cl^- currents resulted in diminished spontaneous and drastically reduced pheromone-evoked spiking of VSNs. Although this indicated an important role of anoctamin channels in VNO signal amplification, the lack of this amplification did not alter VNO-dependent male–male territorial aggression in olfactory *Ano1*/*Ano2* double knockout mice. We conclude that Ano1 mediates the bulk of Ca^{2+}-activated Cl^- currents in the VNO and that Ano2 plays only a minor role. Furthermore, vomeronasal signal amplification by CaCCs appears to be dispensable for the detection of male-specific pheromones and for near-normal aggressive behavior in mice.

In some animals, the vomeronasal organ (VNO)[3] plays an important role in social behaviors such as mating, flight, or aggression. Its sensory cells, the vomeronasal sensory neurons (VSNs), detect pheromones that are released by individuals of the same species or kairomones released by predators and that prompt animals to either attract or avoid each other (1, 2). Extensive research on the murine VNO has shown that it is crucial for various innate social actions. For example, male–male aggression in mice is almost completely abolished when the VNO is ablated (3–5) or when its key signaling components are genetically disrupted (6–9). Moreover, the Bruce effect, an innate pregnancy block when pregnant females encounter a male different from the one they mated with, is diminished in mice lacking the VNO (10, 11), yet some pheromone-induced social behaviors do not require a functional VNO (12), possibly because also other olfactory subsystems may be able to detect pheromones (1).

VSNs are bipolar neurons that possess one unbranched dendrite that protrudes apically into the vomeronasal lumen. At their apical ends, they feature a dendritic knob from which mucus-embedded microvilli emerge. Microvilli and dendritic knobs are the sites where the VNO receptor potential is generated. Whereas dendritic knobs of all VSNs are located at the apical surface of the vomeronasal sensory epithelium (VNE), their cell bodies are organized in an apical and a basal layer. Single VSNs express receptors from two large G protein–coupled receptor families. Cell bodies of vomeronasal receptor type I–expressing VSNs reside within the apical layer and express the G protein subunit $G\alpha_{i2}$, whereas vomeronasal receptors type II–positive VSNs are found in the basal layer of the sensory epithelium and express the G protein subunit $G\alpha_o$ (1). Pheromones bind to microvilli of VSNs and thereby trigger the dissociation of the respective G protein complex. Their β- and γ-subunits then activate phospholipase C, which converts phosphatidylinositol 4,5-bisphosphate into diacylglycerol and

This work was supported in part by Deutsche Forschungsgemeinschaft Grants JE164/10-1 (to T. J. J.) and SFB 894 (to F. Z.) and a NeuroCure Cluster of Excellence grant (to T. J. J.). The authors declare that they have no conflicts of interest with the contents of this article.
This article contains Table S1 and Figs. S1–S4.
[1] Lichtenberg Professor of the Volkswagen Foundation.
[2] To whom correspondence should be addressed: FMP/MDC, Robert-Rössle-Strasse 10, D-13125 Berlin, Germany. Fax: 49-30-9406-2960; E-mail: Jentsch@fmp-berlin.de.

[3] The abbreviations used are: VNO, vomeronasal organ; CaCC, Ca^{2+}-activated Cl^- channel; VSN, vomeronasal sensory neuron; VNE, vomeronasal sensory epithelium; TRPC, transient receptor potential canonical; MOE, main olfactory epithelium; OMP, olfactory marker protein; PSTH, poststimulus time histogram; BES, *N*,*N*-bis[2-hydroxyethyl]-2-aminoethanesulfonic acid.

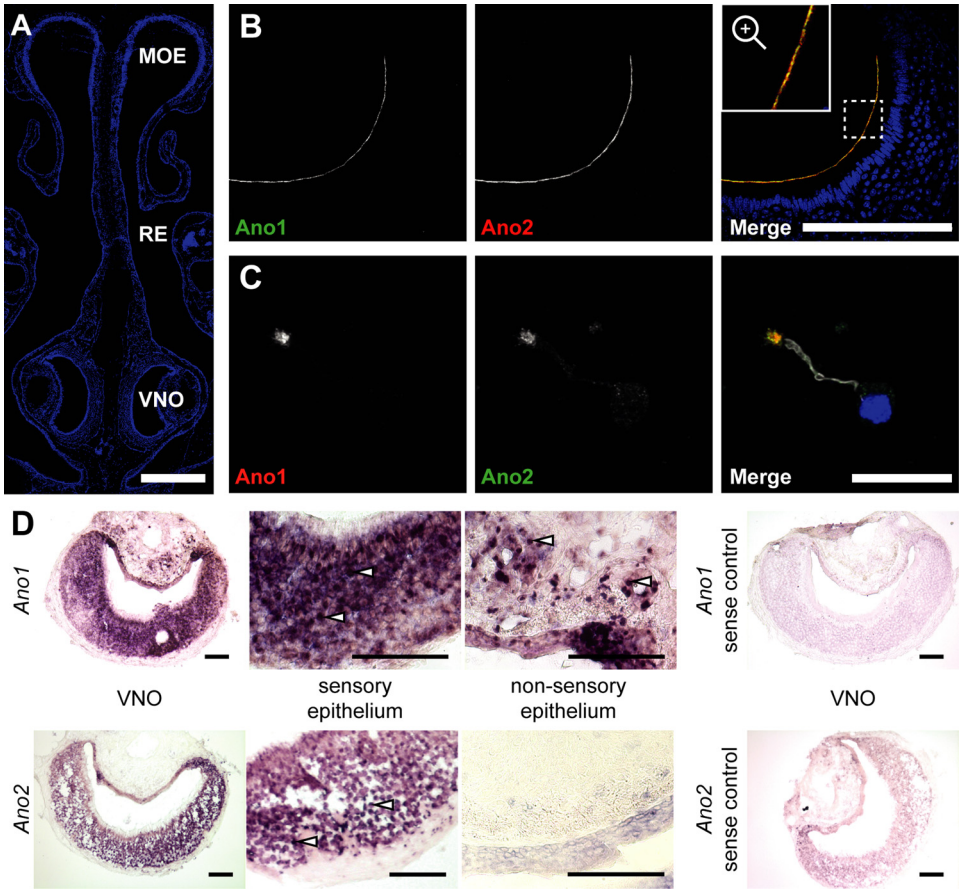

Figure 1. Co-localization of Ano1 and Ano2 in vomeronasal sensory neurons. *A*, 4′,6-diamino-2-phenylindole-stained coronal section of the nose showing the morphology of the murine nasal cavity with MOE, respiratory epithelium (*RE*), and VNO. *Bar*, 500 μm. *B*, coronal sections of the VNO immunolabeled for Ano1 (*green*) and Ano2 (*red*, gpAno2_C1-3) at the apical border of the vomeronasal sensory epithelium. *Bar*, 200 μm. The region marked with a *dashed square* is magnified in the *inset*. *C*, immunostainings of isolated VSNs labeled for Ano1 (*red*), Ano2 (*green*, gpAno2_C1-3), and acetylated tubulin (*white*) at a single dendritic knob. *Bar*, 20 μm. The nuclei are colored *blue* in merged images. *D*, *in situ* hybridizations in coronal VNO slices using a probe against *Ano1* or *Ano2* with respective sense control hybridizations. Higher magnification images of the sensory and nonsensory epithelium are shown; see *white arrows* for examples of single cell bodies. All *bars*, 100 μm.

inositol 1,4,5-triphosphate. Diacylglycerol opens Na^+- and Ca^{2+}-permeable transient receptor potential canonical 2 (TRPC2) channels and thereby depolarize VSNs (13, 14). Several lines of evidence using Cl^--sensitive dyes and perforated patch clamp suggest a high Cl^- concentration inside VSN dendrites (15–17). Ca^{2+} entering through TRPC2 opens Ca^{2+}-activated Cl^- channels (CaCCs) (18), resulting in an efflux of chloride that further depolarizes the cell and may amplify the initial TRPC2–mediated VSN response (17, 19). The incomplete disruption of VNO function observed in TRPC2 knockout mice suggests an alternative activation pathway that bypasses TRPC2. It was postulated that it involves inositol 1,4,5-triphosphate–mediated Ca^{2+} release from intracellular stores and downstream activation of CaCCs, but this explanation was questioned recently (20). We and others have shown previously that the CaCCs anoctamin 1 and 2 (Ano1 and Ano2, or TMEM16A and TMEM16B) are co-expressed in the apical border of the vomeronasal sensory epithelium (21, 22). Although a constitutive knockout of Ano1 is postnatally lethal in mice, likely because of a malformation of the trachea (23), $Ano2^{-/-}$ mice did not show a severe phenotype (22).

Here we confirm the co-expression and co-localization of Ano1 and Ano2 in the microvilli of murine VSNs. Surprisingly, Ano1 carries the bulk of Ca^{2+}-activated Cl^- currents ($I_{Cl(Ca)}$) in VSNs, whereas Ano2 apparently plays only a minor role. Disruption of both channels in mouse VSNs resulted in diminished spontaneous and pheromone-evoked action potential firing. The loss of CaCCs, however, did not result in altered pheromone-induced territorial aggressiveness in male mice.

Results

Expression of Ano1 and Ano2 in the vomeronasal organ

Immunolabeling of paraffin sections of the mouse nose (Fig. 1*A*) showed that Ano1 and Ano2 co-localize close to the dendritic knob of VSNs and line the apical side of the sensory epithelium (Fig. 1*B*), in agreement with previous results (21, 22). Immunostaining of isolated VSNs consistently showed co-expression of both proteins. No cells expressing only one of these channels were detected (Fig. 1*C*). Co-staining for ezrin, a protein expressed on microvilli of VNO-supporting cells (24), showed a dotted intermittent expression pattern at the apical border of the sensory epithelium that neither co-localized with Ano1 nor with Ano2 (Fig. S1, *A* and *B*). Conversely, villin, which is also present in microvilli of VSNs, co-localized with Ano1 (not shown) and Ano2 (Fig. S1*C*).

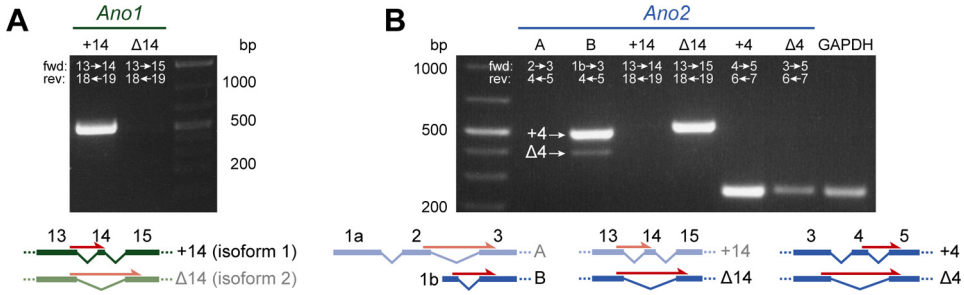

Figure 2. Splice isoforms of Ano1 and Ano2 in the VNO. *A* and *B*, RT-PCR on VNO tissue probing different *Ano1* (*A*) or *Ano2* (*B*) isoforms. The *white numbers* indicate target exons of forward (*fwd*) and reverse (*rev*) primers hybridizing to the spliced-together exons. Schematic drawings of the respective transcript variants are shown below, exon-spanning forward primers are indicated as *red arrows*, and variants that were not detected in the VNO are *faded*. Transcripts of the ubiquitously expressed enzyme glyceraldehyde-3-phosphate dehydrogenase (*GAPDH*) were amplified as positive control.

Hence, the expression of either channel is restricted to microvilli of VSNs.

Because in VSNs the subcellular localization of either channel is almost completely restricted to microvilli, immunohistochemistry is ill suited to examine whether these channels are differentially expressed in apical or basal VSNs. We therefore addressed this issue by *in situ* hybridization that detects *Ano1* and *Ano2* transcripts in the cell bodies of VSNs. Hybridization of coronal VNO cryosections showed an even distribution of *Ano1* and *Ano2* mRNAs across both layers of the VNO sensory epithelium (Fig. 1*D*). *Ano1*-positive cells were also detected in the nonsensory epithelium, which agrees with the localization of Ano1-expressing mucus-secreting glandular cells and vascular smooth muscle cells in the VNO (1). Negative controls using sense RNA probes for *Ano1* or *Ano2* gave no staining (Fig. 1*D*).

Both Ano1 and Ano2 display various splice variants that differ in their biophysical properties (25–36). To determine which splice variants are present in the VNO, we performed RT-PCR on VNO tissue using primers that span exon boundaries and therefore hybridize only to spliced-together exons (see exon labels in Fig. 2). This analysis revealed that vomeronasal transcripts of *Ano1* included exon 14 (Fig. 2*A*). Murine *Ano2* mRNA was previously analyzed in tissue from the eye and the main olfactory epithelium (MOE) (26, 36). Although an *Ano2* isoform including exon 1a and exon 2 was found in the retina (later termed isoform A), in the MOE *Ano2* is predominantly transcribed using an alternative start site at exon 1b while skipping exon 1a-2 (termed isoform B). A nonfunctional variant of isoform B that lacks exon 4 (termed isoform BΔ4; Fig. 2*B*) is also expressed in the MOE (25). While our RT-PCR experiments revealed no expression of the retinal *Ano2* isoform A in the VNO, *Ano2* isoform B was present with and without exon 4. No *Ano2* isoform containing exon 14 could be detected (Fig. 2*B*). Control experiments showed the expression of *Ano2* isoform A in the eye and a lack of *Ano2* in the liver (Fig. S2*A*). Sequencing of cDNAs from the VNO confirmed the existence of an exon 4-containing *Ano2* mRNA. Additionally, a sequence overlap in the chromatogram revealed the co-expression of a variant lacking this alternatively spliced exon (Fig. S2*B*).

Disruption of Ano1 and Ano2 in olfactory epithelia

To investigate the functional roles of CaCCs in the VNO, we generated mouse lines in which Ano1, Ano2, or both are absent from VSNs. Because constitutive deletion of *Ano1* in mice is postnatally lethal, likely because of malformation of the trachea (23), we disrupted *Ano1* specifically in mature olfactory neurons of the various olfactory subsystems. Floxed Ano1 mice (38) were crossed to mice expressing Cre recombinase under the promotor of the olfactory marker protein (OMP) (39) to yield olfactory-specific *Ano1* knockout mice (subsequently called $\Delta Ano1^{olf}$). As expected, Ano1 immunoreactivity was absent from the apical part of the sensory epithelium in the VNO of $\Delta Ano1^{olf}$ mice, whereas Ano2 expression was not affected (Fig. 3*A*). Western blots of *N*-deglycosylated VNO lysates confirmed that Ano2 expression levels were unchanged in the VNO of $\Delta Ano1^{olf}$ (Fig. 3*B*).

Ano1/2 olfactory double knockout mice ($\Delta(Ano1^{olf}/Ano2)$) were obtained by crossing $\Delta Ano1^{olf}$ mice to constitutive $Ano2^{-/-}$ (ΔAno2) mice. We have described ΔAno2 mice previously (22). VNO tissue lysates from WT, $\Delta Ano1^{olf}$, ΔAno2, or $\Delta(Ano1^{olf}/Ano2)$ animals were analyzed by Western blotting. A sharp band corresponding to a nonglycosylated shortened Ano1 protein (lacking the ~6 kDa large part encoded by the floxed exon (38)) appeared in VNO lysates from $\Delta Ano1^{olf}$ and $\Delta(Ano1^{olf}/Ano2)$ mice, but not in those from WT and ΔAno2 animals (Fig. 3*C*). The remaining upper Ano1 band in $\Delta Ano1^{olf}$ lysates likely stems from nonneuronal glandular or vascular smooth muscle cells which do not express OMP. A broad band corresponding to glycosylated Ano2 was detected in lysates from WT and $\Delta Ano1^{olf}$ animals but was absent in ΔAno2 and $\Delta(Ano1^{olf}/Ano2)$ lysates (Fig. 3*C*). Absence of the respective proteins was also seen when staining coronal paraffin sections of the nose from WT and $\Delta(Ano1^{olf}/Ano2)$ mice. Whereas Ano1 and Ano2 immunoreactivity was detected in WT mice and co-localized with villin at the microvillar endings of VSNs, it was absent in $\Delta(Ano1^{olf}/Ano2)$ animals (Fig. 3*D*). The antibody for Ano1 showed some unspecific staining in VSN cell bodies that persisted in the $\Delta Ano1^{olf}$. Expression and localization of villin was not changed in $\Delta(Ano1^{olf}/Ano2)$ VNOs, indicating that microvilli of VSN dendritic knobs are intact. Moreover, gross morphological differences concerning the size, shape, and integrity of the VNO layers, as well as changed expression of VNO marker proteins such as ezrin, TRPC2, $G\alpha_o$, and phosphodiesterase type 4A (PDE4A) could not be observed in $\Delta(Ano1^{olf}/Ano2)$ animals (Fig. 3*D* and Fig. S3*C*).

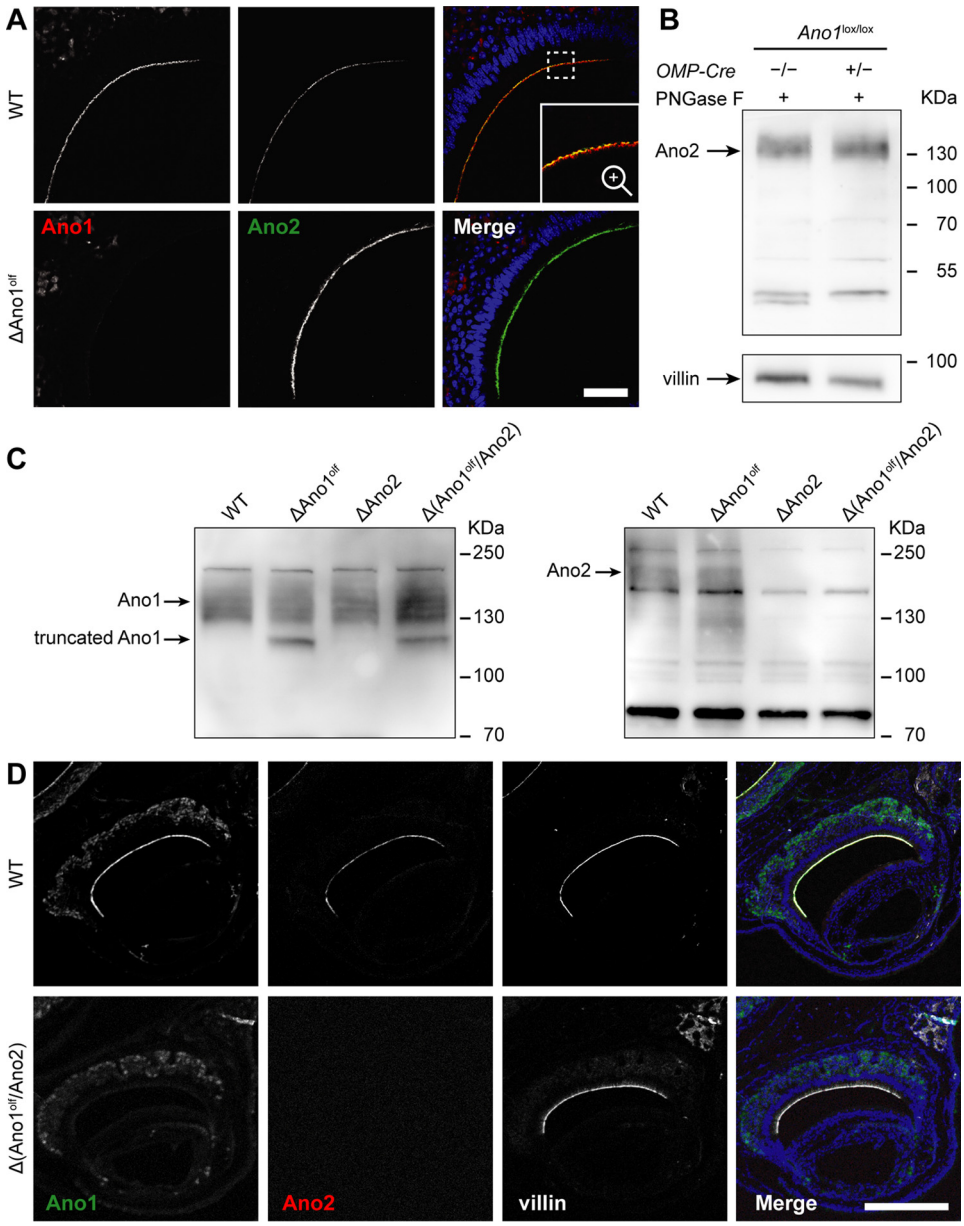

Figure 3. Olfactory double knockout of Ano1 and Ano2. *A*, coronal VNO sections immunolabeled for Ano2 (*green*, gpAno2_C1-3) and Ano1 (*red*) of WT and ΔAno1^{olf} animals. *Bar*, 50 μm. The region marked by the *dashed square* in *A* is magnified in the *inset*. Nuclei are colored *blue* in merged images. *B*, Western blotting for Ano2 (rbAno2_C1-2) of *N*-deglycosylated complete VNO lysates; genotypes are indicated. An *arrow* indicates the expected height of deglycosylated Ano2. Protein load was 20–30 μg per lane. *C*, immunoblots of complete VNO tissue lysates probing Ano1 and Ano2 (rbAno2_N3-3). Genotypes are indicated above. *Arrows* indicate the expected height of the respective protein (glycosylated Ano1: ~130 kDa, glycosylated Ano2: ~200 kDa) and its truncated unglycosylated version (truncated Ano1: ~111 kDa). Protein load: 40 μg per lane. *D*, coronal VNO sections immunolabeled for Ano1 (*green*) and Ano2 (*red*, gpAno2_C1-3) of WT and Δ(Ano1^{olf}/Ano2) animals. Microvilli were stained with villin (*white*). The animals were 59 weeks old. *Bars*, 250 μm. Nuclei are colored *blue* in merged images.

Ca^{2+}-activated Cl^- currents in the VNO

Ca^{2+}-activated Cl^- currents of VSNs were examined in acute slices of the VNO by patching somata in the whole-cell voltage clamp configuration. Recordings with 1.5 μM free [Ca^{2+}] in the pipette revealed robust outwardly rectifying steady-state $I_{Cl(Ca)}$ (with 94.8 ± 15.9 pA/pF at +120 mV (mean ± S.E.)) that exhibited slow voltage-dependent activation at positive potentials in most cells (Fig. 4, *A* and *B*). As expected, these currents were absent in Δ(Ano1^{olf}/Ano2) VSNs (Fig. 4*A*), even when pipette [Ca^{2+}] was increased to 13 μM (Fig. 4*B*). Surprisingly, also VSNs deficient in only Ano1 lacked $I_{Cl(Ca)}$ (Fig. 4, *A* and *C*), whereas ΔAno2 VSNs showed currents with amplitude, rectification and kinetics comparable with those of WT cells (Fig. 4, *A* and *D*, and Fig. S4). Similar results were found when analyzing $I_{Cl(Ca)}$ tail currents (Fig. S4). These results indicate that Ano1 carries the bulk of $I_{Cl(Ca)}$ in sensory neurons of the VNO.

Stimulus-evoked spiking in VSNs

To assess the hypothesis that CaCCs amplify the initial TRPC2-mediated inward current (2, 17, 19), we compared spontaneous and stimulus-evoked spiking in VSNs of WT and

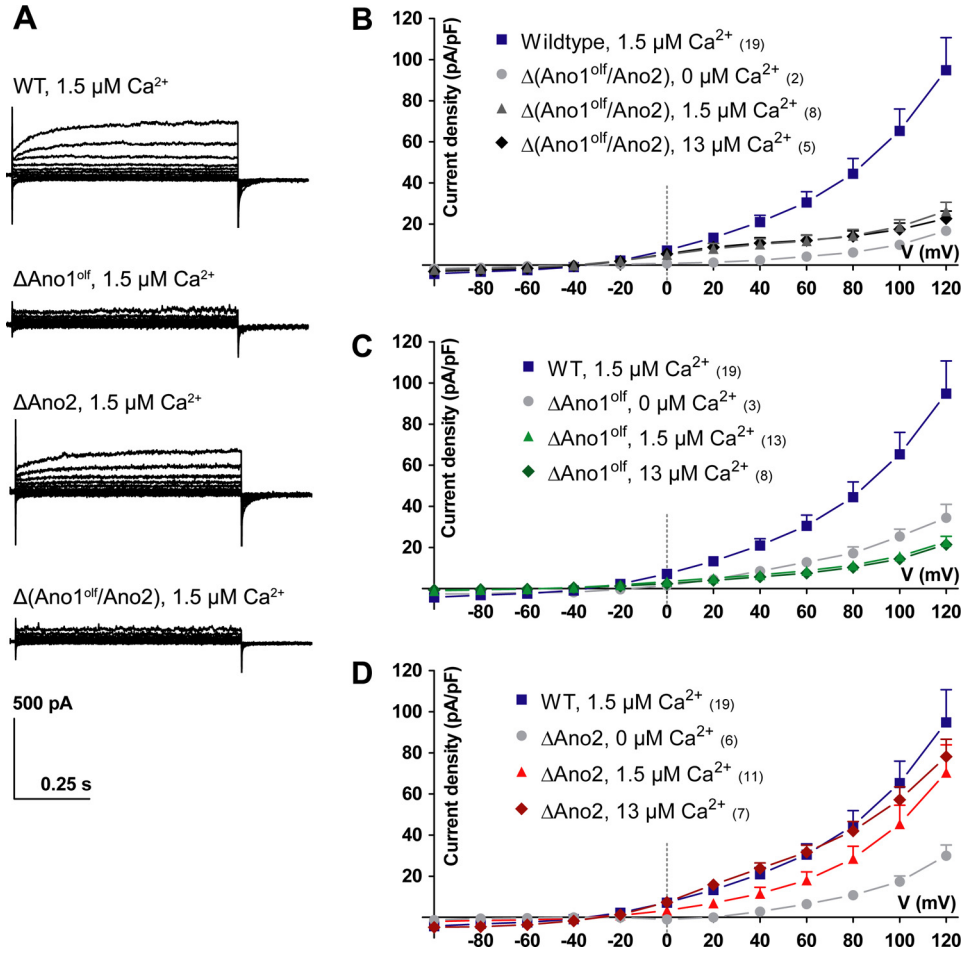

Figure 4. Steady-state Ca^{2+}-activated Cl^- currents in vomeronasal sensory neurons. Steady-state Ca^{2+}-activated Cl^- currents of VSNs in acute slices from the VNO recorded in the whole-cell voltage clamp configuration are shown. Free intracellular Ca^{2+} concentrations in the patch pipette are indicated. *A*, example current traces at different voltage steps (−100 to 120 mV in steps of 20 mV); genotypes are indicated. *B–D*, current density–voltage plots of Ca^{2+}-activated Cl^- currents measured in different genotypes with either 0, 1.5, or 13 μM free Ca^{2+} in the patch pipette. The data from WT VSNs is plotted as reference. *Numbers* in *parentheses* indicate the number of measured cells. Mean current densities at respective voltage steps + S.E. (for clarity, shown only in positive direction).

Δ(Ano1^{olf}/Ano2) animals in the loose-patch configuration. In WT mice 35 of 123 cells (28.5%, 13 mice) showed spontaneous spiking within the baseline observation period of 35 s. However, only 15 of 106 VSNs lacking Ano1 and Ano2 (14.2%, 10 mice) showed spontaneous action potential firing (Fig. 5*A*, *left panel*). Next, we examined stimulus-evoked spiking by applying diluted urine of male mice (pooled from 7 male mice, 1:200 in bath solution) to the microvilli of some of the measured VSNs. In WT animals, 20 of 82 VSNs (24.4%) showed an increase in the action potential firing rate upon urine application. In contrast, only 7 of 90 Δ(Ano1^{olf}/Ano2) VSNs (7.8%) responded to the stimulus (Fig. 5*A*, *right panel*). Representative original spike registrations of stimulated WT and Δ(Ano1^{olf}/Ano2) VSNs that displayed at least one action potential are presented in a raster plot over time in Fig. 5*B* (*upper panels*). Poststimulus time histograms (PSTHs) of all stimulated cells show a mild but clear increase in spiking upon urine stimulation in WT, but not in CaCC-deficient VSNs (Fig. 5*B*, *lower panels*). Firing frequencies of all measured cells before and during the stimulation period were calculated showing that loss of CaCCs resulted in a drastic decrease of pheromone-induced VSN activation (Fig. 5*C*).

CaCCs in VNO-dependent behavior

Because of the marked effect of CaCC ablation on VSN spiking, we asked whether CaCC-mediated signal amplification is of physiological relevance in behaving animals. We assessed male–male territorial aggression, an innate, VNO-dependent behavior in rodents (3–5), by a classical resident–intruder assay (Fig. 6). The number of attacks against an intruder did not significantly differ between WT (9.5 ± 12.4 attacks, mean ± S.D.) and Δ(Ano1^{olf}/Ano2) residents (15.9 ± 16.0 attacks); neither did the summated duration of the attacks (WT: 32.6 ± 47.1 s, Δ(Ano1^{olf}/Ano2): 62.4 ± 65.5 s) nor the average duration of a single attack (WT: 3.3 ± 2.1 s, Δ(Ano1^{olf}/Ano2): 3.9 ± 1.6 s). Moreover, mice lacking CaCCs did not take longer to identify the intruder as indicated by similar values for latency of the first attack (WT: 347 ± 181 s, Δ(Ano1^{olf}/Ano2): 284 ± 221 s) and the sniffing time before the first attack (WT: 80.2 ± 35.5 s, Δ(Ano1^{olf}/Ano2): 67.7 ± 54.1 s). Neither total time of investigative sniffing was altered in Δ(Ano1^{olf}/Ano2) (140 ± 98 s) compared with WT mice (132 ± 61 s). We neither observed differences between Δ(Ano1^{olf}/Ano2) and WT in the time course of aggressive or investigative behavior (Fig. 6*B*).

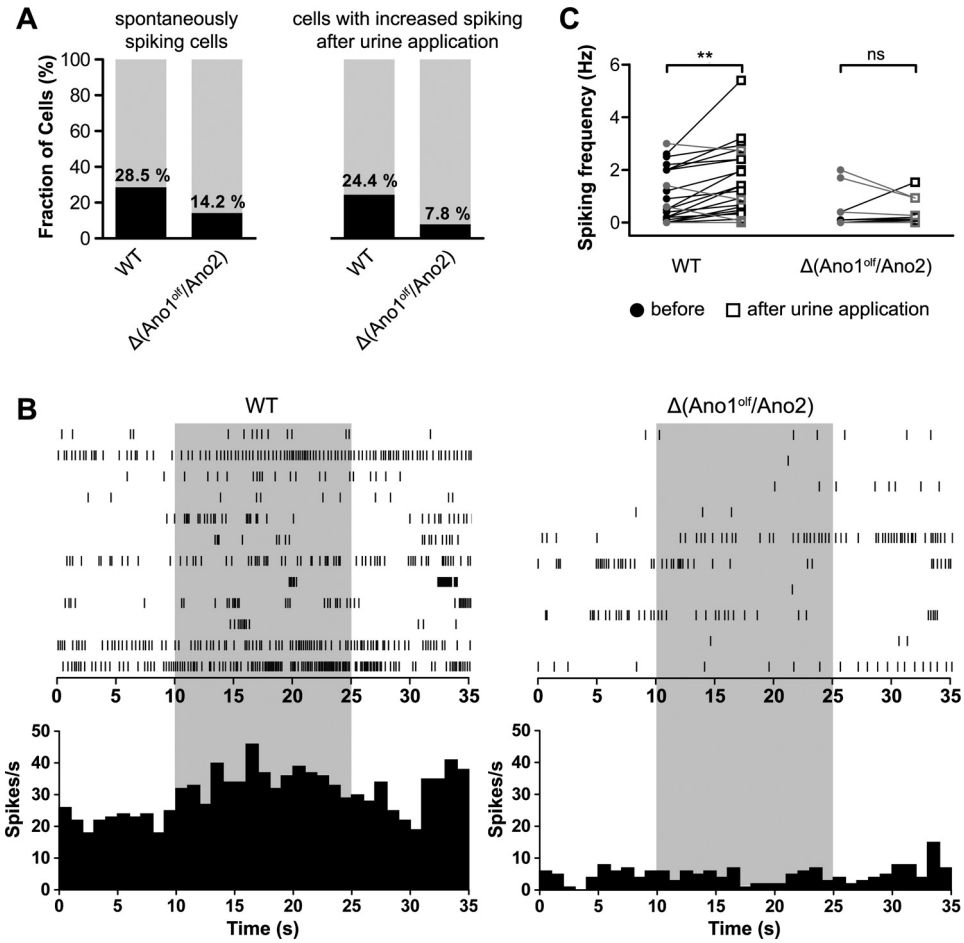

Figure 5. Stimulus-evoked spiking of vomeronasal sensory neurons. *A*, graphical representation of spontaneously firing cells among all recorded VSNs (*left panel*) and cells responsive to the urine stimulus among all stimulated VSNs (*right panel*); genotypes are indicated. *B*, raster plots (*upper panels*) and PSTHs (*lower panels*) of spiking in WT and Δ(Ano1^{olf}/Ano2) VSNs upon stimulation with urine (1:200, indicated in *light gray*). Raster plot of WT does not show all recorded cells for clarity; PSTHs include data of all cells. *C*, VSN firing frequency before (*filled circles*, 0–10 s) and upon stimulation with diluted urine (1:200, *white squares*, 10–25 s). Only data from VSNs that displayed at least one action potential during the recording period are shown (WT: 20 of 82 cells, Δ(Ano1^{olf}/Ano2): 7 of 90 cells). Connected data points were recorded from the same VSN. The cells that showed increased firing are indicated in *black*; others are in *gray*. Increase is significant in WT ($p < 0.0005$) but insignificant in Δ(Ano1^{olf}/Ano2). Paired samples *t* test was used. *ns*, $p > 0.05$ (not significant); **, $p \leq 0.01$.

Discussion

Ano1 and Ano2 co-localization in microvilli of VSNs

Using immunohistochemical labeling with knockout-controled antibodies (22, 40), we showed that Ano1 and Ano2 are lining the apical part of the vomeronasal epithelium and are co-expressed on microvilli of isolated VSNs. This finding agrees with Dibattista *et al.* (21) who demonstrated that Ano1 and Ano2 are co-expressed in single isolated VSNs of either layer. We extended these studies by showing an even distribution of both *Ano1* and *Ano2* mRNA across the different layers of the VNO using *in situ* hybridization.

These data do not rule out an additional expression in supporting sustentacular cells of the VNE as suggested previously (15). However, such an expression is excluded for Ano1 because neuronal-specific OMP-Cre-mediated *Ano1* knockout completely abolished Ano1 immunoreactivity of VNO microvilli. The situation is less clear for Ano2, which was knocked out constitutively. However, Ano2 did not co-localize with ezrin, a marker protein of microvilli of supporting cells (24). Moreover, a presence of Ano2 in supporting cells would be unexpected because to date murine Ano2 was exclusively found in neuronal cells (22, 26, 41–44). Hence Ano1 and Ano2 are co-expressed in microvilli of apical and basal VSNs without evidence for a preferential expression in one of these layers.

Ca^{2+}-activated Cl^- currents in VSNs

Based on the measurement of only a small number of cells, our laboratory previously reported the absence of $I_{Cl(Ca)}$ in most, but not all, VSNs of ΔAno2 animals (22). Recordings of steady-state Ca^{2+}-activated Cl^- currents in the present work were performed in acute slices of the VNO to preserve the native environment of VSNs as much as possible. Unlike in our previous report (22), we now patched cells at their somata and not at dendritic knobs to obtain a larger number of stable recordings. Currents were elicited with 1.5 μM free [Ca^{2+}] in the pipette to activate both Ano1 and Ano2, which differ in their Ca^{2+} sensitivity (EC_{50} for activation of 0.4–0.6 μM and 1–3 μM Ca^{2+}, respectively (27, 36, 45, 46)). Their biophysical properties such as outward rectification and deactivation upon repolarization matched those of heterologously co-expressed Ano1 and Ano2. However, deactivation was faster and slower compared with heterologously expressed Ano1 and Ano2,

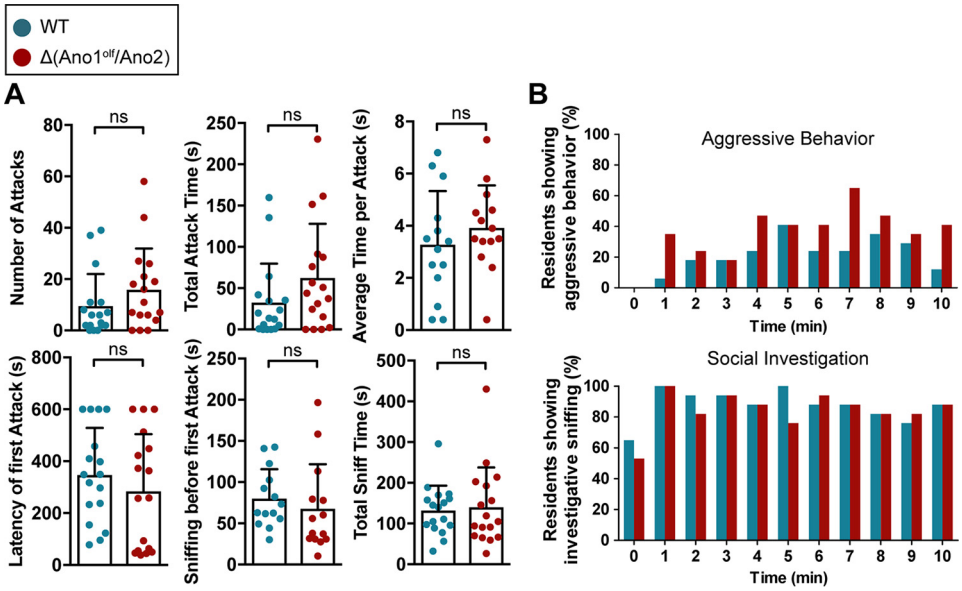

Figure 6. Pheromone-evoked male–male territorial aggression. Male territorial aggressive behavior assessed in a resident–intruder experiment with male residents of indicated genotypes (WT: *turquoise*, $n = 17$ mice; Δ(Ano1^{olf}/Ano2): *red*, $n = 17$ mice). *A*, scatter plots of single experiments showing the number of male–male attacks, the total duration of attacks, the average time per attack, the latency of the first attack, the sniffing time before the first attack, and the total time of investigative sniffing. *Bars* indicate means ± S.D., Mann–Whitney test of significance. *ns*, $p > 0.05$ (not significant). *B*, the time course of the resident's aggressive behavior (*upper panel*) and investigative sniffing behavior (*lower panel*) is represented in histograms indicating the fraction of mice showing the respective behavior at a given time point.

respectively (data not shown). This apparent discrepancy may result from difficulties of fitting exponentials to the small endogenous $I_{Cl(Ca)}$ currents. The disappearance of $I_{Cl(Ca)}$ in Δ(Ano1^{olf}/Ano2) mice unambiguously demonstrates that native Ca^{2+}-activated Cl^- currents of the VNO are meditated by Ano1, Ano2, or both.

Conditional knockout of *Ano1* abolished Ca^{2+}-activated Cl^- currents in VSNs, whereas disruption of *Ano2* only insignificantly reduced them. Consistent with these results, a lack of $I_{Cl(Ca)}$ in isolated VSNs from conditional *Ano1* knockout mice has been reported previously (47). Taken together, this indicates that Ano1 might be responsible for the bulk of native $I_{Cl(Ca)}$ in VSNs. Still, the lack of $I_{Cl(Ca)}$ in *Ano1* knockout VSNs comes as a surprise because we and others clearly showed that the CaCC Ano2 is co-expressed with Ano1 in WT VSNs (21, 22, 24) and that its expression is unchanged in ΔAno1^{olf} VNOs (this work). Moreover, immunostaining did not reveal major differences of Ano2 expression between the VNO and the MOE (22).

A possible explanation for this unexpected finding might be that in our experiments, microvillar [Ca^{2+}] did not reach the levels that are required to activate Ano2, which has a ~4-fold higher EC_{50} for Ca^{2+} compared with the more Ca^{2+}-sensitive Ano1 (27, 36, 45, 46). This hypothesis is supported by our finding that the current–voltage relationship of $I_{Cl(Ca)}$ did not show the typical change from outward rectification to ohmic behavior (22, 46, 48, 49) upon increasing pipette [Ca^{2+}] to 13 μM. Likewise, recordings performed by Amjad *et al.* (47) with 2 mM Ca^{2+} in the pipette did not show a complete linearization of the current-voltage relationship. Cytosolic calcium in dendritic knobs and microvilli may not reach the levels present in the pipette because of diffusional constraints, extensive cytosolic Ca^{2+} buffering or efficient Ca^{2+} extrusion (50).

Others suspected that Ano2 might be expressed as the non-functional isoform BΔ4 in the VNO (47). Although we found *Ano2* BΔ4 transcripts in the VNO, we also detected mRNA that included exon 4 and thus encodes functional Ano2 channels. We found no evidence for the recently proposed scenario (15) in which functional isoforms of Ano2 are only expressed in supporting cells because we did not detect Ano2 in those cells. Because we cannot exclude that Ano2 mediates minor chloride currents in VSNs, we investigated the physiological role of CaCCs in the VNO using mice lacking both Ano1 and Ano2 in VSNs (Δ(Ano1^{olf}/Ano2) mice).

CaCCs in vomeronasal signaling amplification

Since their first description in the early 1990s, Ca^{2+}-activated Cl^- currents were postulated to have an important role in amplifying olfactory signals in the MOE (51). We and others showed that Ano2 is responsible for a large part of the odorant-evoked olfactory current and enhances the initial CNG-dependent depolarization (22). Likewise, CaCCs in VSNs might enhance the depolarization that is initially mediated by TRPC2. Consistent with this idea, we have now shown that lack of CaCCs results in less spontaneous and drastically diminished stimulus-evoked spiking of VSNs. This finding agrees with experiments that used pharmacological blocking of Cl^- channels by niflumic acid or SITS in WT and *Trpc2*$^{-/-}$ VSNs (19). Reduced spontaneous firing was also reported for *Ano2*$^{-/-}$ olfactory sensory neurons of the MOE (52), where spontaneous spiking is likely initiated by basally active olfactory receptors (53, 54). Likewise, basally active vomeronasal receptors may mediate the commonly observed spontaneous firing of VSNs (19, 55–59), and a lack of CaCCs may lead to a less efficient conversion of basal activity into action potentials.

CaCC-mediated amplification is dispensable for male aggression

Surgical ablation of the VNO (3–5) and constitutive disruption of *Trpc2* (6, 7) almost completely suppresses aggressiveness in males. However, reports of reduced VNE thickness in $Trpc2^{-/-}$ mice (7, 19) hint at previously unknown role of TRPC2 in the development or maintenance of the VNO. Similarly, mice deficient for the G proteins $G\alpha_o$ and $G\alpha_{i2}$ display structural differences of the VNE and reduced aggression in the resident–intruder assay (8, 9). Here we showed that loss of both Ano1 and Ano2 resulted in neither a reduced level nor an altered time course of male–male territorial aggression in $\Delta(Ano1^{olf}/Ano2)$ mice. This suggests either that the depolarization caused by Trpc2 channels suffices for these aggressive behaviors or that the structural changes in the VNE observed in $Trpc2^{-/-}$ mice (7, 19) play an important role in the abrogation of aggressiveness. Another reason for the discrepancy between the apparent effect of CaCC loss in our electrophysiological measurements and no impact on the aggressive behavior could be the compensatory action of depolarizing K^+ currents (60) or other pheromone-sensing olfactory subsystems (1). We conclude that CaCCs are unnecessary for the correct development of the VNO and that CaCC-mediated amplification of VSN signaling is dispensable for the detection of male-specific pheromones, which elicits rivaling aggressiveness.

In summary, our work shows that Ca^{2+}-activated Cl^- currents in VSNs are almost exclusively mediated by Ano1 (TMEM16A), although VSNs express significant levels of Ano2 (TMEM16B). Although these Cl^- currents enhance the spontaneous and urine-evoked spontaneous action potential firing of VSNs, supporting their postulated role in amplifying olfactory signals, we could not detect corresponding behavioral deficits. These results resemble those we have obtained with Ano2 in the MOE (22). Whereas Ano2 currents strongly amplified the depolarizing currents in olfactory sensory neurons, no olfactory deficits could be detected in highly sensitive automated tests (22). Later work reported differences in identifying novel odors (52, 61, 62). However, because these differences between WT and $Ano2^{-/-}$ mice disappeared with repeated trials (52, 61), effects of the central nervous system cannot be excluded. In the future, more specialized or sensitive behavioral tests may reveal a physiological role of anoctamins in vomeronasal neurons.

Experimental procedures

Mice

Animal care and experiments conformed to German animal protection laws and were approved by the Berlin authorities (LaGeSo). Conditional olfactory-specific *Ano1* knockout mice ($Ano1^{lox/lox}$, $OMP\text{-}Cre^{+/-}$; $\Delta Ano1^{olf}$) were generated by crossing floxed Ano1 mice (38) with mice expressing Cre recombinase under the endogenous promotor for the OMP (39) in knock-in mice. To avoid a loss of OMP expression, this locus was kept heterozygous ($OMP\text{-}Cre^{+/-}$). $\Delta(Ano1^{olf}/Ano2)$ mice lacking both Ano1 and Ano2 in olfactory neurons ($Ano1^{lox/lox}$, $Ano2^{-/-}$, $OMP\text{-}Cre^{+/-}$) were generated by crossing conditional $\Delta Ano1^{olf}$ mice with constitutive $Ano2^{-/-}$ mice (22). All mice were back-crossed with C57BL/6 to minimize genetic variations among litters.

Tissue lysate preparation, deglycosylation, and immunoblotting

VNO, MOE, or lung tissue was dissected, minced, and sonicated in lysis buffer (150 mM NaCl, 20 mM HEPES, 5 mM EDTA, 1x Roche Complete® protease inhibitor mixture, 1% SDS, pH 7.4) as described (22). For deglycosylation VNO lysates were supplemented with 5% β-mercaptoethanol and preincubated at 55 °C for 15 min. After the addition of *N*-glycosidase F (Roche) and Complete® protease inhibitor in deglycosylation buffer (50 mM HEPES, pH 7.4, 10 mM EDTA, 0.5% Nonidet P-40), the lysates were incubated at 37 °C for 4 h. Total protein concentration of lysates was determined using a microplate reader (ASYS HITECH GmbH) and the Pierce BCA protein assay kit (Pierce). Proteins were separated on SDS-polyacrylamide gels and transferred on polyvinylidene difluoride or nitrocellulose membranes. Primary antibodies were incubated at 4 °C for 24 h with following dilutions: rbAno2_N3-3 rabbit polyclonal (1:1000 (22)); rbAno2_C1-2 rabbit polyclonal (1:500 (22)); anti-TMEM16A (Ano1) rabbit polyclonal (1:100, ab53212, Abcam, its specificity had been shown using $Ano1^{-/-}$ tissue (40)); anti-villin mouse monoclonal (1:1000, SM1373P, antibodies-online.com); anti–α-tubulin mouse monoclonal (1:2000, clone B-5-1-2, T5168, Sigma–Aldrich). Chemiluminescence of horseradish peroxidase coupled secondary antibodies (Chemicon) and SuperSignal West Pico/Femto ECL (Pierce) was detected with a Chemi-Smart 5000 CCD camera system (PeqLab) and the ChemiCapt 5000 software (PeqLab).

Immunohistochemistry

Tissue preparation and immunohistochemical staining was performed as described previously (22). To isolate VSNs, the dissected VNO was digested with collagenase A at a final enzyme concentration of 1 mg/ml for 10 min at room temperature and then for 15 min at 37 °C. After centrifugation the cells were resuspended in Ringer's solution and transferred to a poly-L-lysine/concanavalin A, type V-coated coverslip and kept for at least 1 h at 4 °C. Antibodies were used at the following dilutions: gpAno2_C1-3 guinea pig polyclonal (1:100 (22)); anti-TMEM16A (Ano1) rabbit polyclonal (1:100, ab53212, Abcam); anti-acetylated tubulin mouse monoclonal (1:1000, clone 6-11B-1, T7451, Sigma–Aldrich); anti-ezrin mouse monoclonal (1:250, GTX24069, GeneTex); anti-villin mouse monoclonal (1:2000, SM1373P, antibodies-online.com); anti-$G\alpha_o$ rabbit polyclonal (1:100, Sc-387, Santa Cruz); and anti-PDE4A rabbit polyclonal (1:200, ab14607, Abcam). Detection was carried out using secondary antibodies coupled to Alexa fluorophores (Invitrogen). The nuclei were stained with 4′,6-diamidino-2-phenylindole (1:5000). All confocal images were taken with a Zeiss LSM 510 META or LSM 880 laser scanning microscope using ZEN software (Zeiss) and a Plan-Apochromat 63×/1.40 Oil DIC M27 or EC Plan-Neofluar 10×/0.3 M27 objective (Zeiss).

In situ hybridization

The protocol for *in situ* hybridization was adapted and modified from previous protocols (63, 64). Briefly, mice were sacrificed by CO_2 intoxication and decapitated. The complete VNO inside the bony capsule was removed and further dissected in ice-cold PBS treated with 0.1% (v/v) diethylpyrocarbonate. The soft VNO tissue was immediately embedded in TissueTek O.C.T. compound (Sakura), and 16-μm cryosections were cut. Digoxigenin-labeled *in situ* hybridization was performed as described previously (37). The following primers were used for synthesis of RNA hybridization probes from murine cDNA: *Ano1*, CCACAGCCCGTGCCAGTCAC (forward) and GCCGACCAACAAACCGGCCT (reverse); and *Ano2*, TTACCAAAATCGAGGTTCCG (forward) and AACCTCCTGGTCGAACTGTG (reverse).

RT–PCR

The mice were sacrificed by CO_2 intoxication and decapitated. The complete VNO inside the bony capsule was removed and further dissected in ice-cold diethylpyrocarbonate-treated PBS. Extreme care was taken to exclude the contamination of the VNO with parts of the surrounding MOE. The soft VNO tissue was frozen in liquid nitrogen before further processing with small scissors. Tissue samples of eye and liver were immediately transferred to a ceramic potter embedded into dry ice and ground. Subsequent RNA isolation was performed with the RNeasy mini kit (Qiagen) according to the manufacturer's protocol. 1 μg of purified RNA was used for cDNA transcription with Superscript II reverse transcriptase and random primers (Invitrogen). A parallel reaction without transcriptase (referred to as −RT in this work) was performed and used as a negative control for all RT-PCRs. Following a 30-min RNase H (Roche) digestion at 37 °C, a 25-μl PCR (hybridization temperature: 60 °C, elongation time: 30 s, cycle number: 30) was set up with 1 μl of the cDNA template, 0.2 μM of each primer, and 0.6 μl of OptiTaq polymerase (Roboklon). DNA bands were separated on a 2% agarose gel and visualized by ethidium bromide. Exon spanning primers were designed to exclude an amplification of remaining genomic DNA in the sample (Table S1). Flanking primers are indicated with the respective exons they span separated by an arrow (*e.g.* 2 → 3) in Fig. 2 and Fig. S2.

Electrophysiological measurements

6–25-week-old mice were sacrificed by CO_2 intoxication and decapitated. The complete VNO inside the bony capsule was removed and further dissected in ice-cold oxygenated Ringer's (140 mM NaCl, 5 mM KCl, 10 mM glucose, 1 mM sodium pyruvate, 10 mM HEPES, pH 7.4, 2 mM $CaCl_2$, 1 mM $MgCl_2$; osmolality adjusted to 320 mOsm/kg with glucose; used for all whole cell current measurements) or S1 solution (125 mM NaCl, 25 mM $NaHCO_3$, 5 mM BES, pH 7.3, 5 mM KCl, 1 mM $CaCl_2$, 1 mM $MgSO_4$; osmolality adjusted to 320 mOsm/kg with glucose; used for all spiking measurements) under a stereo microscope. The dissected soft VNO tissue was embedded into 4% low melting agarose in Ringer's or S1 solution and cut into 150–200-μm-thick slices with a Leica VT1200S vibratome. The slices remained in cold oxygenated Ringer's or S1 solution for at least 1 h until used for the experiment. Patch pipettes were pulled from borosilicate glass (Hilgenberg) by a DMZ-Universal Puller (Zeitz Instruments) with a typical resistance of 3–5 MΩ. The cells were visually selected using an upright light microscope (Olympus BX50WI) and a 40× water immersion objective. For whole-cell measurements, pipettes were filled with a solution containing 100 mM CsMSF, 40 mM CsCl, 10 mM HEPES (pH 7.2), 5 mM EGTA, 4 mM Na_2-ATP, and 1 mM $MgCl_2$. Free Ca^{2+} concentrations of 0, 1.5, and 13 μM were calculated according to the Maxchelator program and set with a 1 M $CaCl_2$ stock solution. A GΩ seal was established at the soma of the VSN for steady-state voltage clamp measurements of Ca^{2+}-activated Cl^- currents. During recordings, tissue slices were superfused with oxygenated Ringer's solution, supplied with 10 mM tetraetylammonium to block potassium currents. Steady-state chloride currents were measured in the whole-cell configuration with a MultiClamp 700B amplifier, Digidata 1440 digitizer, and pClamp 10 software (Molecular Devices) at a sampling frequency of 10 kHz and with 6 kHz low-pass filtering. The membrane was clamped to potentials between −100 and +120 mV in steps of 20 mV for 750 ms following a 250-ms repolarization step to −100 mV. Between test protocols, the cell was held at −30 mV for up to 30 min. Morphological integrity of all VSNs was assessed by including Alexa Fluor 488 dye (Invitrogen) in the pipette solution and visual inspection of the fluorescence. Loose patch measurements on VSN somata were done to record spiking events in acute VNO slices. Bath and pipette contained S1 solution oxygenated with carbogen (95% O_2, 5% CO_2). Seal resistances were between 30 and 80 MΩ. After baseline recording at 0 pA for 35 s, the VSN's microvilli were stimulated by a 15-s application of diluted urine (1:200 pooled urine from sexually naïve C57BL/6 male mice in bath solution) containing Alexa Fluor 488 dye (Invitrogen) for visualization. The application pipette was placed ~20–50 μm away from the dendritic knob and connected to a pressure application system (Toohey Instruments) triggered by pClamp 10 software (Molecular Devices). Electrophysiological data were analyzed with pClamp 10 (Molecular Devices), Matlab 2012b (Mathworks), and self-written scripts in R. Poststimulus time histograms were calculated with a self-written script in R. Spiking frequency was calculated by dividing the number of spiking events (detected through a threshold-based event search with pClamp 10) by the time of the prestimulation (0–10 s) or stimulation period (10–25 s), respectively. To exclude contamination of tail current densities by fast capacitive current transients, an exponential curve was fitted to the tail current, and the initial current density at time point 0 after the depolarization step was extrapolated for each recorded current trace. The Ca^{2+}-dependent component of this tail current was extracted by subtracting the mean current density obtained with 0 μM free Ca^{2+} in the respective genotype. To obtain the deactivation time constants τ, tail currents were fitted to a monoexponential term ($f(t) = e^{-t/\tau} + c$ where t indicates time, τ indicates deactivation constant, and c indicates constant) using pClamp 10. Monoexponential curves were fitted to the tail currents because they were too small to reliably obtain time constants from bi-exponential fits. Graphs and statistics analysis were made with Prism 5 (GraphPad).

Resident–intruder aggression test

Male aggression was assessed by performing the resident–intruder assay as described previously (8) with slight modifications. Male resident mice were single-housed for 7 days prior to the test. During that time, the bedding of the cage was not changed to allow habituation of the mouse in the home cage. On the test day, a castrated male mouse (intruder) was put into the home cage. To ensure a standard stimulus consistent among all single encounters, the intruder was marked with 50 μl of pooled urine collected previously from adult, sexually naïve C57BL/6 male mice. During the encounter of 10 min, all behavior was recorder with a digital camera. In the following blinded post hoc video analysis using BORIS software (v2.981, University of Torino) and a self-written script in R, following parameters were measured: latency to the first attack (in seconds), number of single attacks, total duration of aggressive behavior (in seconds), average duration of single attacks (in seconds), total time of investigative sniffing behavior (in seconds), and sniffing behavior before the first attack (in seconds). The following actions of the resident against the intruder were counted as attacks: biting, tail flicking, chasing, keeping down. Graphs and statistics analysis (Mann–Whitney test of significance) were made with Prism 5 (GraphPad). Tested resident mice were Δ(Ano1^{olf}/Ano2) animals (*Ano1*$^{lox/lox}$, *OMP-Cre*$^{+/-}$, *Ano2*$^{-/-}$) at an age of 8–22 weeks. The animals were sexually naïve and were group-housed before their isolation. As control, age-matched male mice from the same strain but with either a homozygous WT allele (*Ano2*$^{+/+}$) or a heterozygous allele (*Ano2*$^{+/-}$) for *Ano2* and no expression of the Cre recombinase (*OMP-Cre*$^{-/-}$) were used. All resident mice were homozygous for the floxed *Ano1* allele (*Ano1*$^{flox/flox}$). Intruder mice were castrated C57BL/6 mice obtained from Charles River Laboratories at an age of 8–10 weeks.

Author contributions—J. M., G. B., T. L.-Z., F. Z., and T. J. J. conceptualization; J. M. data curation; J. M. and T. J. J. formal analysis; J. M. validation; J. M. investigation; J. M. and T. J. J. visualization; J. M. and T. J. J. writing-original draft; J. M., G. B., T. L.-Z., F. Z., and T. J. J. writing-review and editing; G. B. and C. A. H. resources; T. L.-Z. and F. Z. methodology; T. J. J. supervision; T. J. J. funding acquisition; T. J. J. project administration.

Acknowledgment—We thank Peter Mombaerts (Max-Planck-Forschungsstelle für Neurogenetik, Frankfurt am Main) for the OMP-Cre mouse line.

References

1. Munger, S. D., Leinders-Zufall, T., and Zufall, F. (2009) Subsystem organization of the mammalian sense of smell. *Annu. Rev. Physiol.* **71,** 115–140 CrossRef Medline
2. Chamero, P., Leinders-Zufall, T., and Zufall, F. (2012) From genes to social communication: molecular sensing by the vomeronasal organ. *Trends Neurosci.* **35,** 597–606 CrossRef Medline
3. Bean, N. J. (1982) Modulation of agonistic behavior by the dual olfactory system in male mice. *Physiol. Behav.* **29,** 433–437 CrossRef Medline
4. Clancy, A. N., Coquelin, A., Macrides, F., Gorski, R. A., and Noble, E. P. (1984) Sexual behavior and aggression in male mice: involvement of the vomeronasal system. *J. Neurosci.* **4,** 2222–2229 CrossRef Medline
5. Maruniak, J. A., Wysocki, C. J., and Taylor, J. A. (1986) Mediation of male mouse urine marking and aggression by the vomeronasal organ. *Physiol. Behav.* **37,** 655–657 CrossRef Medline
6. Leypold, B. G., Yu, C. R., Leinders-Zufall, T., Kim, M. M., Zufall, F., and Axel, R. (2002) Altered sexual and social behaviors in *trp2* mutant mice. *Proc. Natl. Acad. Sci. U.S.A.* **99,** 6376–6381 CrossRef Medline
7. Stowers, L., Holy, T. E., Meister, M., Dulac, C., and Koentges, G. (2002) Loss of sex discrimination and male–male aggression in mice deficient for TRP2. *Science* **295,** 1493–1500 CrossRef Medline
8. Chamero, P., Katsoulidou, V., Hendrix, P., Bufe, B., Roberts, R., Matsunami, H., Abramowitz, J., Birnbaumer, L., Zufall, F., and Leinders-Zufall, T. (2011) G protein Gα_o is essential for vomeronasal function and aggressive behavior in mice. *Proc. Natl. Acad. Sci. U.S.A.* **108,** 12898–12903 CrossRef Medline
9. Norlin, E. M., Gussing, F., and Berghard, A. (2003) Vomeronasal phenotype and behavioral alterations in Gα_{i2} mutant mice. *Curr. Biol.* **13,** 1214–1219 CrossRef Medline
10. Bruce, H. M. (1959) An exteroceptive block to pregnancy in the mouse. *Nature* **184,** 105–105 CrossRef Medline
11. Bellringer, J. F., Pratt, H. P., and Keverne, E. B. (1980) Involvement of the vomeronasal organ and prolactin in pheromonal induction of delayed implantation in mice. *J. Reprod. Fertil.* **59,** 223–228 CrossRef Medline
12. Tirindelli, R., Dibattista, M., Pifferi, S., and Menini, A. (2009) From pheromones to behavior. *Physiol. Rev.* **89,** 921–956 CrossRef Medline
13. Lucas, P., Ukhanov, K., Leinders-Zufall, T., and Zufall, F. (2003) A diacylglycerol-gated cation channel in vomeronasal neuron dendrites is impaired in TRPC2 mutant mice: mechanism of pheromone transduction. *Neuron* **40,** 551–561 CrossRef Medline
14. Leinders-Zufall, T., Storch, U., Bleymehl, K., Mederos, Y., Schnitzler, M., Frank, J. A., Konrad, D. B., Trauner, D., Gudermann, T., and Zufall, F. (2018) PhoDAGs enable optical control of diacylglycerol-sensitive transient receptor potential channels. *Cell Chem. Biol.* **25,** 215–223 CrossRef Medline
15. Untiet, V., Moeller, L. M., Ibarra-Soria, X., Sánchez-Andrade, G., Stricker, M., Neuhaus, E. M., Logan, D. W., Gensch, T., and Spehr, M. (2016) Elevated cytosolic Cl^- concentrations in dendritic knobs of mouse vomeronasal sensory neurons. *Chem. Senses* **41,** 669–676 CrossRef Medline
16. Kim, S., Ma, L., Unruh, J., McKinney, S., and Yu, C. R. (2015) Intracellular chloride concentration of the mouse vomeronasal neuron. *BMC Neurosci.* **16,** 90–90 CrossRef Medline
17. Yang, C., and Delay, R. J. (2010) Calcium-activated chloride current amplifies the response to urine in mouse vomeronasal sensory neurons. *J. Gen. Physiol.* **135,** 3–13 CrossRef Medline
18. Zufall, F., Ukhanov, K., Lucas, P., Liman, E. R., and Leinders-Zufall, T. (2005) Neurobiology of TRPC2: from gene to behavior. *Pflügers Arch.* **451,** 61–71 Medline
19. Kim, S., Ma, L., and Yu, C. R. (2011) Requirement of calcium-activated chloride channels in the activation of mouse vomeronasal neurons. *Nat. Commun.* **2,** 365 CrossRef Medline
20. Chamero, P., Weiss, J., Alonso, M. T., Rodríguez-Prados, M., Hisatsune, C., Mikoshiba, K., Leinders-Zufall, T., and Zufall, F. (2017) Type 3 inositol 1,4,5-trisphosphate receptor is dispensable for sensory activation of the mammalian vomeronasal organ. *Sci. Rep.* **7,** 10260 CrossRef Medline
21. Dibattista, M., Amjad, A., Maurya, D. K., Sagheddu, C., Montani, G., Tirindelli, R., and Menini, A. (2012) Calcium-activated chloride channels in the apical region of mouse vomeronasal sensory neurons. *J. Gen. Physiol.* **140,** 3–15 CrossRef Medline
22. Billig, G. M., Pál, B., Fidzinski, P., and Jentsch, T. J. (2011) Ca^{2+}-activated Cl^- currents are dispensable for olfaction. *Nat. Neurosci.* **14,** 763–769 CrossRef Medline
23. Rock, J. R., Futtner, C. R., and Harfe, B. D. (2008) The transmembrane protein TMEM16A is required for normal development of the murine trachea. *Dev. Biol.* **321,** 141–149 CrossRef Medline
24. Dauner, K., Lissmann, J., Jeridi, S., Frings, S., and Möhrlen, F. (2012) Expression patterns of anoctamin 1 and anoctamin 2 chloride channels in the mammalian nose. *Cell Tissue Res.* **347,** 327–341 CrossRef Medline
25. Ponissery Saidu, S., Stephan, A. B., Talaga, A. K., Zhao, H., and Reisert, J. (2013) Channel properties of the splicing isoforms of the olfactory calci-

um-activated chloride channel anoctamin 2. *J. Gen. Physiol.* **141,** 691–703 CrossRef Medline
26. Stöhr, H., Heisig, J. B., Benz, P. M., Schöberl, S., Milenkovic, V. M., Strauss, O., Aartsen, W. M., Wijnholds, J., Weber, B. H., and Schulz, H. L. (2009) TMEM16B, a novel protein with calcium-dependent chloride channel activity, associates with a presynaptic protein complex in photoreceptor terminals. *J. Neurosci.* **29,** 6809–6818 CrossRef Medline
27. Ferrera, L., Caputo, A., Ubby, I., Bussani, E., Zegarra-Moran, O., Ravazzolo, R., Pagani, F., and Galietta, L. J. (2009) Regulation of TMEM16A chloride channel properties by alternative splicing. *J. Biol. Chem.* **284,** 33360–33368 CrossRef Medline
28. Hwang, S. J., Blair P. J., Britton, F. C., O'Driscoll, K. E., Hennig, G., Bayguinov, Y. R., Rock, J. R., Harfe, B. D., Sanders, K. M., and Ward, S. M. (2009) Expression of anoctamin 1/TMEM16A by interstitial cells of Cajal is fundamental for slow wave activity in gastrointestinal muscles. *J. Physiol.* **587,** 4887–4904 CrossRef Medline
29. Davis, A. J., Forrest, A. S., Jepps, T. A., Valencik, M. L., Wiwchar, M., Singer, C. A., Sones, W. R., Greenwood, I. A., and Leblanc, N. (2010) Expression profile and protein translation of TMEM16A in murine smooth muscle. *Am. J. Physiol. Cell Physiol.* **299,** C948–C959 CrossRef Medline
30. Ferrera, L., Scudieri, P., Sondo, E., Caputo, A., Caci, E., Zegarra-Moran, O., Ravazzolo, R., and Galietta, L. J. (2011) A minimal isoform of the TMEM16A protein associated with chloride channel activity. *Biochim. Biophys. Acta* **1808,** 2214–2223 CrossRef Medline
31. Ubby, I., Bussani, E., Colonna, A., Stacul, G., Locatelli, M., Scudieri, P., Galietta, L., and Pagani, F. (2013) TMEM16A alternative splicing coordination in breast cancer. *Mol. Cancer* **12,** 75–75 CrossRef Medline
32. Caputo, A., Caci, E., Ferrera, L., Pedemonte, N., Barsanti, C., Sondo, E., Pfeffer, U., Ravazzolo, R., Zegarra-Moran, O., and Galietta, L. J. (2008) TMEM16A, a membrane protein associated with calcium-dependent chloride channel activity. *Science* **322,** 590–594 CrossRef Medline
33. Tian, Y., Schreiber, R., and Kunzelmann, K. (2012) Anoctamins are a family of Ca^{2+}-activated Cl^- channels. *J. Cell Sci.* **125,** 4991–4998 CrossRef Medline
34. Sondo, E., Scudieri, P., Tomati, V., Caci, E., Mazzone, A., Farrugia, G., Ravazzolo, R., and Galietta, L. J. (2014) Non-canonical translation start sites in the TMEM16A chloride channel. *Biochim. Biophys. Acta* **1838,** 89–97 CrossRef Medline
35. Xiao, Q., Yu, K., Perez-Cornejo, P., Cui, Y., Arreola, J., and Hartzell, H. C. (2011) Voltage- and calcium-dependent gating of TMEM16A/Ano1 chloride channels are physically coupled by the first intracellular loop. *Proc. Natl. Acad. Sci. U.S.A.* **108,** 8891–8896 CrossRef Medline
36. Stephan, A. B., Shum, E. Y., Hirsh, S., Cygnar, K. D., Reisert, J., and Zhao, H. (2009) ANO2 is the cilial calcium-activated chloride channel that may mediate olfactory amplification. *Proc. Natl. Acad. Sci. U.S.A.* **106,** 11776–11781 CrossRef Medline
37. Schütze, S., Orozco, I. J., and Jentsch, T. J. (2016) KCNQ potassium channels modulate sensitivity of skin down-hair (D-hair) mechanoreceptors. *J. Biol. Chem.* **291,** 5566–5575 CrossRef Medline
38. Heinze, C., Seniuk, A., Sokolov, M. V., Huebner, A. K., Klementowicz, A. E., Szijartó, I. A., Schleifenbaum, J., Vitzthum, H., Gollasch, M., Ehmke, H., Schroeder, B. C., and Hübner, C. A. (2014) Disruption of vascular Ca^{2+}-activated chloride currents lowers blood pressure. *J. Clin. Invest.* **124,** 675–686 CrossRef Medline
39. Li, J., Ishii, T., Feinstein, P., and Mombaerts, P. (2004) Odorant receptor gene choice is reset by nuclear transfer from mouse olfactory sensory neurons. *Nature* **428,** 393–399 CrossRef Medline
40. Gomez-Pinilla, P. J., Gibbons, S. J., Bardsley, M. R., Lorincz, A., Pozo, M. J., Pasricha, P. J., Van de Rijn, M., West, R. B., Sarr, M. G., Kendrick, M. L., Cima, R. R., Dozois, E. J., Larson, D. W., Ordog, T., and Farrugia, G. (2009) Ano1 is a selective marker of interstitial cells of Cajal in the human and mouse gastrointestinal tract. *Am. J. Physiol. Gastrointest. Liver Physiol.* **296,** G1370–G1381 CrossRef Medline
41. Cherkashin, A. P., Kolesnikova, A. S., Tarasov, M. V., Romanov, R. A., Rogachevskaja, O. A., Bystrova, M. F., and Kolesnikov, S. S. (2016) Expression of calcium-activated chloride channels Ano1 and Ano2 in mouse taste cells. *Pflugers Arch.* **468,** 305–319 CrossRef Medline
42. Ha, G. E., Lee, J., Kwak, H., Song, K., Kwon, J., Jung, S.-Y., Hong, J., Chang, G.-E., Hwang, E. M., Shin, H.-S., Lee, C. J., and Cheong, E. (2016) The Ca^{2+}-activated chloride channel anoctamin-2 mediates spike-frequency adaptation and regulates sensory transmission in thalamocortical neurons. *Nat. Commun.* **7,** 13791–13791 CrossRef Medline
43. Huang, W. C., Xiao, S., Huang, F., Harfe, B. D., Jan, Y. N., and Jan, L. Y. (2012) Calcium-activated chloride channels (CaCCs) regulate action potential and synaptic response in hippocampal neurons. *Neuron* **74,** 179–192 CrossRef Medline
44. Zhang, W., Schmelzeisen, S., Parthier, D., Frings, S., and Möhrlen, F. (2015) Anoctamin calcium-activated chloride channels may modulate inhibitory transmission in the cerebellar cortex. *PLoS One* **10,** e0142160 CrossRef Medline
45. Yang, Y. D., Cho, H., Koo, J. Y., Tak, M. H., Cho, Y., Shim, W.-S., Park, S. P., Lee, J., Lee, B., Kim, B.-M., Raouf, R., Shin, Y. K., and Oh, U. (2008) TMEM16A confers receptor-activated calcium-dependent chloride conductance. *Nature* **455,** 1210–1215 CrossRef Medline
46. Pifferi, S., Dibattista, M., and Menini, A. (2009) TMEM16B induces chloride currents activated by calcium in mammalian cells. *Pflügers Arch.* **458,** 1023–1038 Medline
47. Amjad, A., Hernandez-Clavijo, A., Pifferi, S., Maurya, D. K., Boccaccio, A., Franzot, J., Rock, J., and Menini, A. (2015) Conditional knockout of TMEM16A/anoctamin1 abolishes the calcium-activated chloride current in mouse vomeronasal sensory neurons. *J. Gen. Physiol.* **145,** 285–301 CrossRef Medline
48. Schroeder, B. C., Cheng, T., Jan, Y. N., and Jan, L. Y. (2008) Expression cloning of TMEM16A as a calcium-activated chloride channel subunit. *Cell* **134,** 1019–1029 CrossRef Medline
49. Kuruma, A., and Hartzell, H. C. (1999) Dynamics of calcium regulation of chloride currents in *Xenopus* oocytes. *Am. J. Physiol.* **276,** C161–C175 CrossRef Medline
50. Schwaller, B. (2010) Cytosolic Ca^{2+} buffers. *Cold Spring Harb. Perspect. Biol.* **2,** a004051 Medline
51. Kleene, S. J., and Gesteland, R. C. (1991) Calcium-activated chloride conductance in frog olfactory cilia. *J. Neurosci.* **11,** 3624–3629 CrossRef Medline
52. Pietra, G., Dibattista, M., Menini, A., Reisert, J., and Boccaccio, A. (2016) The Ca^{2+}-activated Cl^- channel TMEM16B regulates action potential firing and axonal targeting in olfactory sensory neurons. *J. Gen. Physiol.* **148,** 293–311 CrossRef Medline
53. Reisert, J. (2010) Origin of basal activity in mammalian olfactory receptor neurons. *J. Gen. Physiol.* **136,** 529–540 CrossRef Medline
54. Connelly, T., Savigner, A., and Ma, M. (2013) Spontaneous and sensory-evoked activity in mouse olfactory sensory neurons with defined odorant receptors. *J. Neurophysiol.* **110,** 55–62 CrossRef Medline
55. Ukhanov, K., Leinders-Zufall, T., and Zufall, F. (2007) Patch-clamp analysis of gene-targeted vomeronasal neurons expressing a defined V1r or V2r receptor: ionic mechanisms underlying persistent firing. *J. Neurophysiol.* **98,** 2357–2369 CrossRef Medline
56. He, J., Ma, L., Kim, S., Schwartz, J., Santilli, M., Wood, C., Durnin, M. H., and Yu, C. R. (2010) Distinct signals conveyed by pheromone concentrations to the mouse vomeronasal organ. *J. Neurosci.* **30,** 7473–7483 CrossRef Medline
57. Kelliher, K. R., Spehr, M., Li, X.-H., Zufall, F., and Leinders-Zufall, T. (2006) Pheromonal recognition memory induced by TRPC2-independent vomeronasal sensing. *Eur. J. Neurosci.* **23,** 3385–3390 CrossRef Medline
58. Leinders-Zufall, T., Brennan, P., Widmayer, P., S, P. C, Maul-Pavicic, A., Jäger, M., Li, X.-H., Breer, H., Zufall, F., and Boehm, T. (2004) MHC class I peptides as chemosensory signals in the vomeronasal organ. *Science* **306,** 1033–1037 CrossRef Medline
59. Leinders-Zufall, T., Lane, A. P., Puche, A. C., Ma, W., Novotny, M. V., Shipley, M. T., and Zufall, F. (2000) Ultrasensitive pheromone detection by mammalian vomeronasal neurons. *Nature* **405,** 792–796 CrossRef Medline
60. Kim, S., Ma, L., Jensen, K. L., Kim, M. M., Bond, C. T., Adelman, J. P., and Yu, C. R. (2012) Paradoxical contribution of SK3 and GIRK channels to the activation of mouse vomeronasal organ. *Nat. Neurosci.* **15,** 1236–1244 CrossRef Medline

61. Neureither, F., Stowasser, N., Frings, S., and Möhrlen, F. (2017) Tracking of unfamiliar odors is facilitated by signal amplification through anoctamin 2 chloride channels in mouse olfactory receptor neurons. *Physiol. Rep.* **5,** e13373 CrossRef Medline
62. Dibattista, M., Pifferi, S., Boccaccio, A., Menini, A., and Reisert, J. (2017) The long tale of the calcium activated Cl^- channels in olfactory transduction. *Channels* **11,** 399–414 CrossRef Medline
63. Schaeren-Wiemers, N., and Gerfin-Moser, A. (1993) A single protocol to detect transcripts of various types and expression levels in neural tissue and cultured cells: *in situ* hybridization using digoxigenin-labelled cRNA probes. *Histochemistry* **100,** 431–440 CrossRef Medline
64. Ishii, T., and Mombaerts, P. (2011) Coordinated coexpression of two vomeronasal receptor V2R genes per neuron in the mouse. *Mol. Cell. Neurosci.* **46,** 397–408 CrossRef Medline

Ca^{2+}-activated Cl^- currents in the murine vomeronasal organ enhance neuronal spiking but are dispensable for male–male aggression

Jonas Münch, Gwendolyn Billig, Christian A. Hübner, Trese Leinders-Zufall, Frank Zufall and Thomas J. Jentsch

J. Biol. Chem. 2018, 293:10392-10403.
doi: 10.1074/jbc.RA118.003153 originally published online May 16, 2018

Supporting Information for

Ca^{2+}-activated Cl^- currents in the murine vomeronasal organ enhance neuronal spiking but are dispensable for male-male aggression

Jonas Münch, Gwendolyn Billig, Christian A. Hübner,
Trese Leinders-Zufall, Frank Zufall, Thomas J. Jentsch

List of Supporting Material

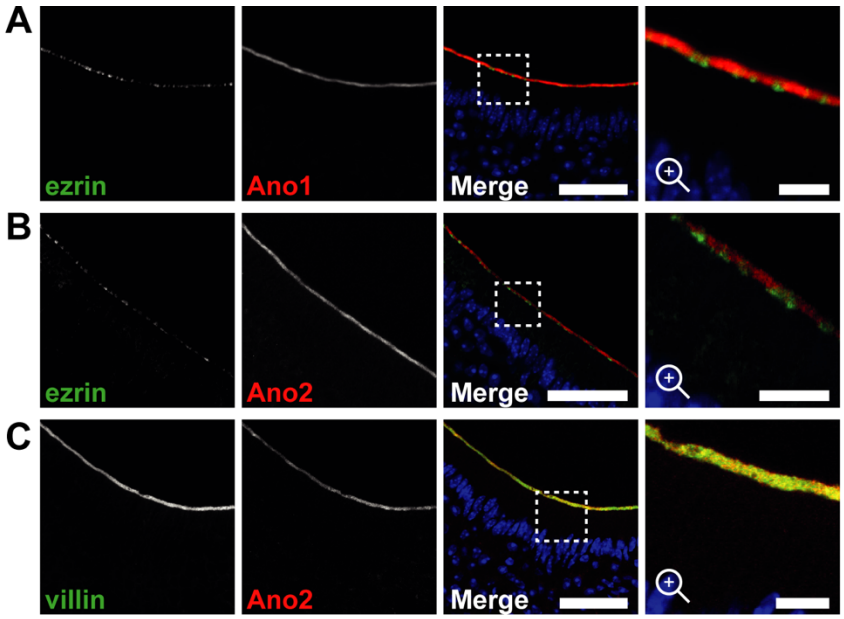

Figure S 1: Colocalization of Ano1 and Ano2 with markers for microvilli

A–B, coronal VNO sections immunolabeled for ezrin (green) shows staining at the apical border of the sensory epithelium which does not colocalize with Ano1 (red) or Ano2 (red, gpAno2_C1-3). Dashed region is magnified. *C*,

villin (green) colocalizes with Ano2 (red, gpAno2_C1-3). Dashed region is magnified. Bars: 100 µm (magnified images: 50 µm). Nuclei are colored blue in merged images.

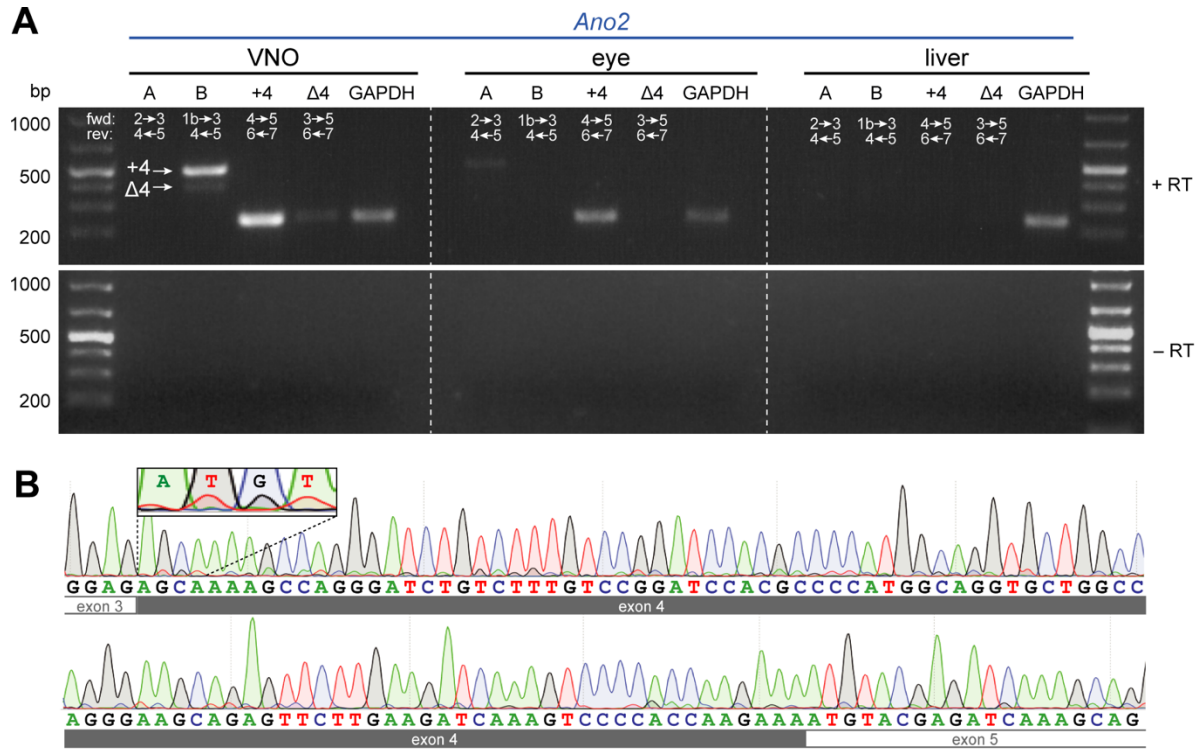

Figure S 2: Splice isoforms of Ano1 and Ano2 in the VNO

A, RT-PCR on VNO tissue probing different *Ano1* or *Ano2* isoforms in VNO, eye and liver tissue, target exons of forward (fwd) and reverse (rev) primers are indicated, the lower part labelled with "–RT" indicates the control RT-PCR without reverse transcriptase. *B*, *Ano2* sequencing chromatogram of cDNA from the VNO, sequence corresponding to exon 4 is indicated in light grey. An overlapping chromatogram sequence corresponding to exon 5 is magnified in the inset.

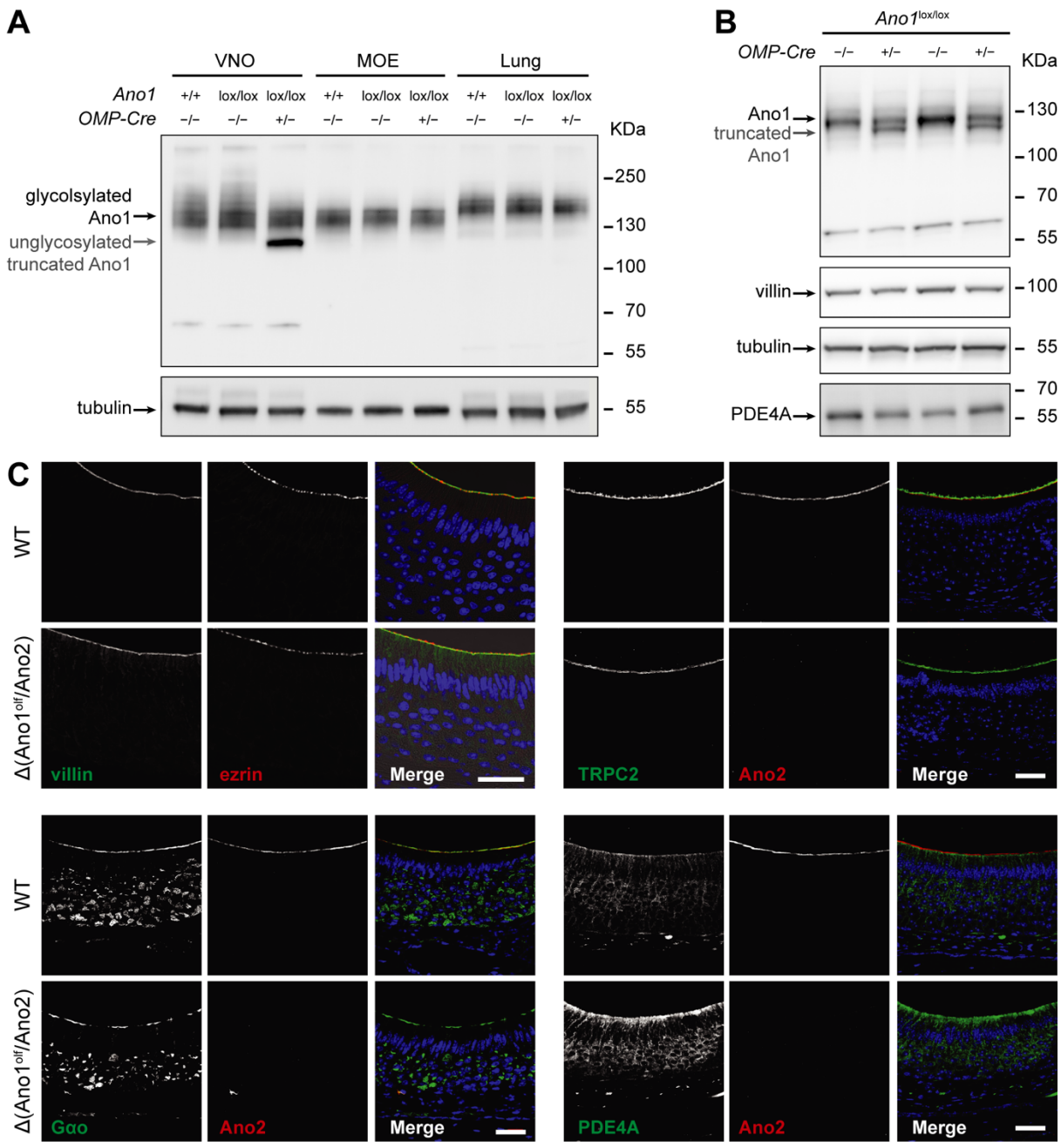

Figure S 3: Olfactory double knock-out of Ano1 and Ano2

A, Western blot for Ano1 of lysates from different tissues and genotypes, protein load per lane: 40 µg (VNO), 20 µg (MOE), 50 µg (lung), tubulin was used as loading control. *B*, Western blot for Ano1 of N-deglycosylated complete VNO lysates (upper blot) and for villin, tubulin and PDE4A, genotypes are indicated, protein load per lane: 20–40 µg. Arrows indicate the band of the respective proteins. *C*, coronal VNO sections immunolabeled for vomeronasal key proteins villin (green) ezrin (red), Gαo (green), TRPC2 (green) and PDE4A (green) in wild-type and Δ(Ano1^{olf}/Ano2) mice. Ano2 (red, gpAno2_C1-3) was costained as reference. Bar: 40 µm. Nuclei are colored blue in merged images.

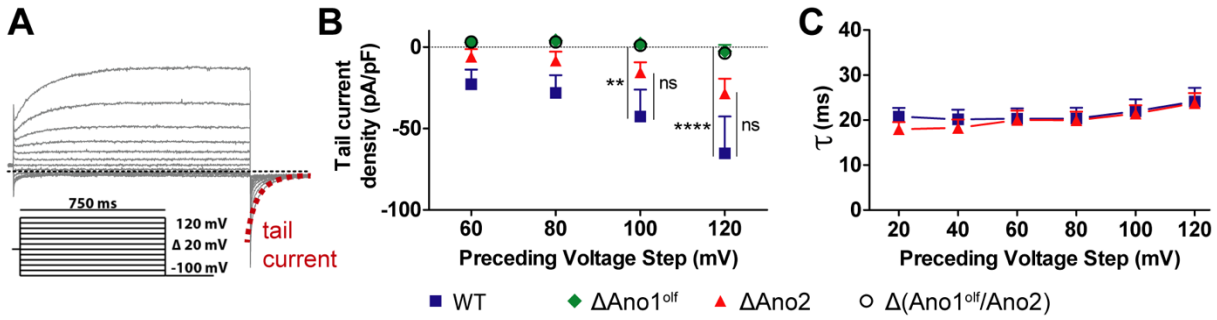

Figure S 4: Ca^{2+}-activated Cl^- tail currents

A, example wild-type voltage clamp current trace demonstrating the tail current curve fit (red dashed line) at the beginning of the −100 mV repolarization step, voltage clamp protocol is shown below. *B*, Ca^{2+}-dependent current density extrapolated from exponential fits of $I_{Cl(Ca)}$ tail currents of wild-type, ΔAno1^{olf}, ΔAno2 and Δ(Ano1^{olf}/Ano2) VSNs. Mean current density after the respective preceding voltage step + SEM, Two-way ANOVA with Bonferroni post-test. ns: $P > 0.05$ (not significant, WT vs. ΔAno2), **: $P \leq 0.01$ (WT vs. ΔAno1^{olf}), ****: $P \leq 0.0001$ (WT vs. ΔAno1^{olf}). *C*, Deactivation time constants τ from mono-exponential fits of $I_{Cl(Ca)}$ tail currents. Mean of deactivation time constant τ at respective preceding voltage steps + SEM. Measured cells: 19 WT, 13 ΔAno1^{olf}, 11 ΔAno2, 8 Δ(Ano1^{olf}/Ano2). Free intracellular Ca^{2+} concentration: 1.5 µM.

Table S1: Primers for RT-PCR

Gene	Label	Primer sequence (5'→3')	PCR product	Remarks[#]
Ano1	+14	GGAGGAGGAGGAAGCTGTCAAGGAT CCGACCAACAAACCGGCCTT	496 bp	exon 13→14→15 to 18←19, targeting isoform 1 including exon 14
Ano1	Δ14	CTTCGAGGAGGAGGAGGATCATCC CCGACCAACAAACCGGCCTT	490 bp	exon 13→15 to 18←19, targeting isoform 2 excluding exon 14
Ano2	A	AGTTCCCGAGACCGTTCTGTCATC CTGAACTTCTTTGCGATGCTGCCT	488 bp	exon 2→3 to 5, targeting isoform A
Ano2	B	CCAGAACACCTGCCAGTCATCAATAA CTGAACTTCTTTGCGATGCTGCCT	485 bp	exon 1b→3 to 5, targeting isoform B
Ano2	+4	CCCCACCAAGAAAATGTACGAG GAATCTCGTGTACAATGCGGCT	233 bp	exon 4→5 to 6←7, targeting isoform including exon 4
Ano2	Δ4	GGAGAAGGACTTGGAGATGTACGAG GAATCTCGTGTACAATGCGGCT	236 bp	exon 3→5 to 6←7, targeting isoform excluding exon 4
Ano2	+14	GGAAGAAGAACGTTCCCAGGAA TCTGCCCACAAACCTCCCCT	523 bp	exon 13→14→15 to 18←19, targeting isoform including exon 14
Ano2	Δ14	GGGATCGAAGAGGAAGAAGAACA TCTGCCCACAAACCTCCCCT	522 bp	exon 13→15 to 18←19, targeting isoform excluding exon 14
GAPDH	GAPDH	ACAGCAACAGGGTGGTGGAC TTTGAGGGTGCAGCGAACTT	ca. 250 bp	targets ubiquitous glyceraldehyde 3-phosphate dehydrogenase as positive control

[#] exon spanning primers were designed to exclude an amplification of remaining genomic DNA in the sample, flanking primers are indicated with the respective exons they span separated by an arrow (e.g. 2→3)